A two-dimensional hybrid model of the Hall thruster discharge

F. I. Parra[a] and E. Ahedo[b]
Escuela Técnica Superior de Ingenieros Aeronáuticos, Universidad Politécnica de Madrid, Plaza Cardenal Cisneros, 28040 Madrid, Spain

J. M. Fife[c]
Air Force Research Laboratory, 1 Ara Road, Edwards AFB, California 94025

M. Martínez-Sánchez[d]
Department of Aeronautics and Astronautics, Massachusetts Institute of Technology, 77 Massachusetts Avenue, Cambridge 02139

Particle-in-cell methods are used for ions and neutrals. Probabilistic methods are implemented for ionization, charge-exchange collisions, gas injection, and particle-wall interaction. A diffusive macroscopic model is proposed for the strongly magnetized electron population. Cross-field electron transport includes wall collisionality and Bohm-type diffusion, the last one dominating in most of the discharge. Plasma quasineutrality applies except for space-charge sheaths, which are modeled taking into consideration secondary-electron-emission and space-charge saturation. Specific weighting algorithms are developed in order to fulfil the Bohm condition on the ion flow at the boundaries of the quasineutral domain. The consequence is the full development of the radial plasma structure and correct values for ion losses at lateral walls. The model gains in insight and physical consistency over a previous version, but thrust efficiency is lower than in experiments, indicating that further model refinement of some phenomena is necessary. © *2006 American Institute of Physics.* [DOI: 10.1063/1.2219165]

I. INTRODUCTION

There is a strong scientific and technological interest in Hall thrusters, which are one of the most developed concepts in the field of electric space propulsion. Since the first operative Hall thruster was launched to space in the 1970s, this technology has been tested on several flights, and its functionality has been proven enough to consider them a reliable propulsion alternative. The research in this field has focused lately on: the development of thrusters of different power levels, operation at higher or lower specific impulse with minimum penalty on lifetime and performance, and different improvements on basic designs. To these ends, it is crucial to increase the understanding of the plasma physics of these engines and to develop reliable and versatile models of the whole plasma discharge.

Many models of the plasma discharge in a Hall thruster have been proposed in recent years. They can be classified in three main groups: fluid models,[1,2] particle models,[3] and hybrid (fluid/particle) models.[4–6] Kinetic models are used only for particular aspects of the discharge (such as interaction of the plasma with the chamber walls). Hybrid fluid/particle-in-cell(PIC) models represent a good tradeoff between macroscopic and fully PIC ones. They provide numerical solutions

in relatively short times, despite the disparate dynamic scales of electrons and ions, and the relatively complex thruster geometry and magnetic field topology.

Fife and Martínez-Sánchez developed the first two-dimensional (2D) hybrid model, which was called HPHall.[4,7] Heavy species (ions and neutrals) are modeled with PIC plus Monte Carlo (MC)-type methods, whereas electrons are modeled as a fluid. Electrons are strongly magnetized and the high anisotropy introduced by the magnetic field *B* permits decoupling of the solutions of the electron motions perpendicular and parallel to *B*. HPHall was completed in 1998 and has been used in the analysis of several designs and thruster phenomena and as base or input for other codes.[3,8–12] The usefullness of this simulation model, the large experience gained with it, and recent advances in Hall thruster theory and modeling have made it advisable to update and improve HPHall. This paper explains both the fundamental features of the model (as presented in Ref. 7) and the main advances on modelization made recently.

The changes implemented in the present version of the model (which we call HPHall-2) can be classified in two categories. The first category consists of improvements which do not affect the fundamentals of the code but increase its capabilities. The main ones are: (a) implementation of ion-neutral collisions; (b) algorithms for injection, reflection, and recombination of neutrals at the walls; and (c) development of routines to check the local conservation of heavy species magnitudes, such as mass and energy.

The second and main category of changes is related to plasma-wall interaction phenomena, and these improvements were necessary to assure the consistency of the model. A key

[a]Present address: Department of Aeronautics and Astronautics, Massachusetts Institute of Technology, 77 Massachusetts Av., 02139 Cambridge; electronic mail: fparra@mit.edu
[b]Electronic mail: eduardo.ahedo@upm.es
[c]Present address: Exponent 149 Commonwealth Drive, Menlo Park, California 91025; electronic mail: mfife@exponent.com
[d]Electronic mail: mmart@mit.edu

feature of HPHall is that it takes advantage of the small Debye length of the plasma to apply quasineutrality in the bulk of the discharge. This condition drastically reduces the computation time because it avoids the very short spatial and temporal scales associated with space-charge fields. For example, a typical simulation of 1 ms, with 1100 cells and 60 000 particles in a common personal computer takes around 200 min. As a counterpart, this quasineutral model cannot solve the space-charge sheaths formed around the chamber walls. In the zero Debye-length limit, the quasineutral model sees these sheaths as discontinuity surfaces tied to the chamber walls. These sheaths must be solved independently and the plasma conditions to be imposed at the near-wall boundaries of the (quasineutral) computational domain are *not* the wall conditions but the transition conditions to those sheaths.

The advances on the understanding of Hall thruster plasmas in recent years have led us to identify, in the original HPHall, three subjects related to sheath and wall phenomena that required improvements. The first one is the fulfillment by the ion flow of the Bohm condition required by the sheath solution; we discussed this delicate issue in Ref. 13. The second one is the inclusion of the "wall-collisionality" phenomenon in all electron equations, adopting the treatment of Ahedo *et al.*[1] And the third one is the adoption of the sheath model of Ahedo,[15] which distinguishes between primary and secondary electrons and takes into account the space-charge saturation for high secondary electron emission (SEE).

The rest of the paper is organized as follows. Section II presents a description of general aspects of the model. Section III is devoted to the PIC submodel for heavy species. The Bohm condition issue, although part of the PIC submodel, has been treated separately in Sec. IV. Section V is devoted to the macroscopic submodel for electrons. The simulation results presented in Sec. VI are examples of the innovations and capabilities of the code and allow us to discuss the physics of the discharge. Conclusions are presented in Sec. VII.

II. GENERAL FEATURES OF THE HYBRID MODEL

HPHall-2 is an axisymmetric, quasineutral simulation of the plasma discharge between the anode and the cathode (i.e., the neutralization surface). The magnetic field $\boldsymbol{B}$ in the chamber is generated externally by the thruster magnetic circuit and is implemented into the simulation code in a preprocess. The small magnetic field induced by the thruster discharge is disregarded. HPHall-2 is divided into two submodels: a PIC submodel for the heavy species and a macroscopic submodel for the electrons. Both submodels are advanced sequentially in time with a time step Δt. During each time step, the main outputs of the PIC submodel are the plasma density $n_e=n_i$ (only singly charged ions are considered in this paper) and the ion flux density $\boldsymbol{g}_i=n_i\boldsymbol{u}_i$. These values are then used in the electron submodel, which consists of quasineutrality $(n_e=n_i)$, electron mobility and energy equations, and current conservation, to generate ϕ and T_e. The electric field is then calculated from ϕ, which, together with T_e, provides the necessary input for another advance-
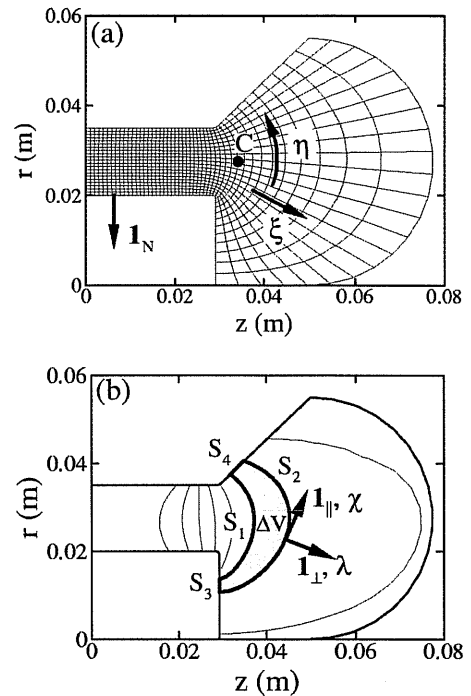

FIG. 1. (a) Mesh and variables used by the PIC submodel for cases 1.1 and 1.2. of Sec. VI. $\boldsymbol{1}_N$ represents a vector perpendicular to the domain boundaries. C is the cathode position. (b) Magnetic streamlines and finite-volumes used by the PIC submodel for cases 1.1 and 1.2.

ment of the PIC submodel. The algorithm continues to iterate in this way until a specified amount of computational time has elapsed.

Cylindrical variables (z,r,θ) describe the physical space. The PIC submodel works with a structured, simulation mesh (ξ,η) in the plane (z,r), Fig. 1. The nodes of the mesh cells correspond to integer values of ξ and η, and are denoted by jk, with j and k the integer parts of ξ and η, respectively. For a conventional thruster geometry, the anodic boundary is at $\xi=1$, and the inner and outer lateral boundaries are at $\eta=1$ and $\eta=k_{max}$, respectively. These lateral boundaries correspond to Debye sheaths next to chamber walls, the plume-ambient interface, or the axis of symmetry. The simulation mesh is created in a pre-process and the code stores the values at the nodes of the transformation $(z,r)=H(\xi,\eta)$ and of its Jacobian matrix $JH(\xi,\eta)$; a bilinear function is used to determine H and JH at cell interior points.

Since electrons are strongly magnetized, a collisional-diffusive model is used with different transport properties in the directions parallel and perpendicular to the magnetic field. A mesh of magnetic streamlines: λ_l, with $l=1,2,\dots,$ (Fig. 1) is used to integrate the electron equations. The magnetic streamlines (indeed, axisymmetric streamsurfaces) are obtained from

$$\partial\lambda/\partial z = rB_r, \quad \partial\lambda/\partial r = -rB_z. \tag{1}$$

The first streamline, λ_1, is one intersecting the anode wall. Since the PIC and magnetic meshes do not coincide generally, plasma magnitudes are interpolated linearly between $\xi=1$ and $\lambda=\lambda_1$. The same is done at the plume boundary. In addition to λ, it is convenient to define an arc variable χ along *each* streamline, which satisfies

$$(\partial z/\partial \chi, \partial r/\partial \chi) = (B_z, B_r)/B. \qquad (2)$$

Notice that χ is defined as the length along the magnetic streamlines and lines of χ=const. are not necessarily perpendicular to lines λ=const. The directional derivative in the directions parallel and perpendicular (in a meridional plane) to the magnetic field, $1_\parallel$ and $1_\perp$ (Fig. 1), are given by

$$\frac{\partial}{\partial 1_\perp} = rB \frac{\partial}{\partial \lambda}, \quad \frac{\partial}{\partial 1_\parallel} = \frac{\partial}{\partial \chi}. \qquad (3)$$

III. THE HEAVY SPECIES SUBMODEL

As a compromise between good statistics and resolution of the strong inhomogeneity of plasma densities along the chamber, the model uses $N^{\text{cell}} \sim 20$–50 (macro)particles per cell and species (i.e., neutral and ions). Ion and neutral densities differ typically by two orders of magnitude. Therefore, to maintain roughly equal numbers of macroneutrals and macroions, the typical mass M_n of a macroneutral is much larger than the mass M_i of a macroion. This has consequences in the collisional processes, particularly for ionization: a single ionizing event cannot transform one macroneutral into one macroion.

The time step Δt is selected so that, in general, one macroion advances no more than one cell per time step. Starting from the plasma state at instant t, the process to determine the number of particles, their mass, position, and velocity at $t + \Delta t$ includes the stages we describe next.

A. Advancement of particles

Let us consider that, at instant t, we know the position x and velocity v of all macroparticles; the plasma density n_e, the electric potential ϕ, the electron temperature T_e, and the magnetic field $B(z, r)$. The equations of particle motion are satisfied using a leapfrog scheme[16]

$$v_{+1/2} - v_{-1/2} = \Delta t \left[\frac{q}{m}(E_0 + v_{-1/2} \wedge B) + R_0 \right], \qquad (4)$$

$$x_1 - x_0 = \Delta t v_{+1/2}, \qquad (5)$$

modified to work on a structured nonuniform axisymmetric mesh. Here, q/m is the particle charge-to-mass ratio (zero for neutrals and e/m_i for ions), v is the particle velocity, E is the electric field, R is any nonelectromagnetic force (such as charge-exchange resistive effects on neutrals), and a numerical subscript a refers to the instant $t + a\Delta t$.

In order to avoid large errors on the position of particles that are close to the axis of symmetry, $r=0$, Eqs. (4) and (5) are solved in a cylindrical frame of reference centered at the position of each particle at instant t.[16] The new position of a particle in the simulation grid (ξ, η, θ) is determined using a Newton's algorithm on function $(z, r) = H(\xi, \eta)$.

B. Ionization

Ionization takes place by electron impact on the neutrals. Direct simulation Monte Carlo (DSMC) methods are not applicable to simulate ionization because the electrons are treated as a fluid.[17] Standard Monte Carlo collisions (MCC)

methods are not applicable either since (i) neutral particles are the dominant species, (ii) the neutral flux is highly reduced along the chamber, and (iii) ion and neutral particles have very different masses. Therefore, a particular method was developed for ionization in HPHall.[7]

The single-charge ionization rate

$$\dot{n}_i = n_n n_e \zeta(T_e), \qquad (6)$$

is obtained assuming a Maxwellian electron distribution function and using the Drawin ionization model $\zeta(T_e)$.[18] For each macroneutral, ionization events during a time interval Δt produce a decay of its mass according to

$$M_n(t + \Delta t) = [1 - \Delta t n_e \zeta(T_e)] M_n(t). \qquad (7)$$

For the same time interval, the number of macroions created by ionization at a generic cell jk is based on the quantity

$$N_{jk,\text{ioniz}} = \frac{m_i}{M_i} \langle \dot{n}_i \rangle V_{jk} \Delta t, \qquad (8)$$

where M_i is the mass of a new macroion, V_{jk} is the cell volume, and $\langle \dot{n}_i \rangle$ is the average ionization rate within the cell. The effective (integer) number of new macroions is determined from a probability algorithm applied on $N_{jk,\text{ioniz}}$. The position (at $t + \Delta t$) within the cell and the velocity (at $t + \Delta t/2$) of these macroions are selected randomly. For the velocity, we use a drifting Maxwellian distribution, based on the *local* fluid velocity and temperature of the neutrals, u_n and T_n, respectively.

C. Ion-neutral collisions

The main phenomenon considered here is the presence of charge-exchange (CEX) collisions. Generally, their effect is more important in the plume, where low-velocity ions can be deflected by the plume potential and hit spacecraft surfaces. HPHall is used as a source model for plume models[19] and a limited CEX algorithm has been implemented in order to estimate the number of low-velocity ions coming from inside the channel.

Charge-exchange collisions keep constant the ion and neutral densities but modify their momentum. Considering the mass difference between macroions and macroneutrals $(M_n \gg M_i)$, a MCC model seems a good option to treat this phenomenon. Light macroions will undergo these collisions individually but heavy macroneutrals will feel them only in an average way.

The basic magnitude modelling CEX collisions is the rate parameter

$$\zeta_{\text{CEX}}(c_{ni}) = \sigma_{\text{CEX}}(c_{ni}) c_{ni},$$

based on the CEX cross section and the macroscopic drift velocity between species, $c_{ni} = u_i - u_n$. The probability that a macroion undergoes a CEX collision is

$$P_{\text{CEX}} = 1 - \exp(-n_n \zeta_{\text{CEX}} \Delta t). \qquad (9)$$

For ions, the model decides probabilistically whether the collision takes place. The new velocity of the macroion is obtained randomly from the drifting Maxwellian distribution

function of neutrals. For each macroneutral, the effect of CEX collisions is the resistive force

$$R_{CEX} = M_n n_i \zeta_{CEX} c_{ni}. \tag{10}$$

The MCC model is acceptable in the thruster channel, because c_n and c_i are similar, or not too dissimilar. In the plume, however, $c_i \gg c_n$, and the CEX collisions create a distinct population of fast neutrals, which MCC ignores. Because of that, plume models usually work with DSMC.[19]

D. Injection of neutrals at the boundaries

Three different processes inject neutrals at different boundaries of the simulation domain: net injection of propellant from the feeding system at the anode, reflection of neutrals at the walls, and recombination of ions at the walls. In addition, at the plume boundaries, there are losses of ions and neutrals and possible injection of ambient neutrals. For each process, wall panel, and time step, probability algorithms are used to determine the number of injected macroneutrals, and the location and injection velocity of each of them.

In general, the gas injector occupies several panels of the anode surface. The number of injected neutrals per panel is proportional to the anode gas flow ($\dot{m}_a$), the time step, and the area of the panel, and is inversely proportional to the total surface of the injector and the mass of a macroneutral at injection ($M_{n,inj}$). At the injector, the gas distribution function is assumed to be a drifting Maxwellian of temperature T_{inj} and average velocity (normal to the injector) u_{inj}. Then, the probability function for the velocity tangential and perpendicular to the injection surface are[16,17]

$$p_t(\boldsymbol{v}_t) = \frac{m_i}{2\pi T_{inj}} \exp\left(-\frac{m_i \|\boldsymbol{v}_t\|^2}{2T_{inj}}\right), \quad \boldsymbol{v}_t \in \mathbb{R}^2, \tag{11}$$

$$p_p(v_p) = \frac{(m_i/T_{inj})v_p \exp[-m_i(v_p - u_{inj})^2/2T_{inj}]}{\exp(-\bar{u}_{inj}^2) + \pi^{1/2}\bar{u}_{inj}\,\mathrm{erfc}(-\bar{u}_{inj})},$$
$$v_p \in [0,\infty[, \tag{12}$$

with $\bar{u}_{inj} = u_{inj}(m_i/2T_{inj})^{1/2}$.

We must distinguish between the reflection of macroneutrals and the recombination of light macroions into heavy macroneutrals. The distribution function for a neutral reflected from a wall panel is a semi-Maxwellian distribution of temperature

$$T_{emi} = a_w T_{wall} + (1 - a_w)T_{imp}, \quad 2T_{imp} = \frac{m_i \sum\limits_p M_p v_p^2}{2 \sum\limits_p M_p}, \tag{13}$$

where a_w is an accommodation coefficient ($a_w = 0.8$ in the simulation examples of this paper), T_{wall} is the wall temperature, T_{imp} is the "temperature" of the neutrals impacting the panel, which is determined from the impact velocity v_p, and summation index p extends to all neutrals impacting the panel within a time step.

Due to the mass disparity, the recombination of one macroion at the wall cannot lead to the creation of one macroneutral. Instead, the model defines the probability of injecting back a macroneutral as the total mass of ions impacting one panel within a given time step divided by the mass selected for the new macroneutral $M_{n,inj}$. If a macroneutral is finally injected, the point of injection is decided randomly and the probability function for the injection velocity is the same as for a reflected neutral, except that T_{imp} in Eq. (13) is based now on the velocity of impacting ions.

E. Weighting of plasma magnitudes

Once the mass, position, and velocity of all ions and neutrals are known at instants $t + \Delta t$ or $t + \Delta t/2$, we must proceed to weight macroscopic magnitudes for each species to each node jk of the simulation mesh. In order to distribute the properties of each macroparticle among the neighboring nodes, we use the first-order weighting function

$$S_{jk}(\xi, \eta) = \begin{cases} (1 - |\xi'|)(1 - |\eta'|), & (\xi', \eta') \in I, \\ 0, & (\xi', \eta') \notin I, \end{cases} \tag{14}$$

with $\xi' = \xi - j$ and $\eta' = \eta - k$ and $I = [-1,1] \times [-1,1]$.

Density, particle flux, macroscopic velocity, pressure (tensor), and temperature (tensor) of a given species (ions or neutrals) at node jk are computed from

$$n_{jk} = \frac{1}{m_i \Omega_{jk}} \sum_p S_{jk}(\xi_p, \eta_p) M_p, \tag{15}$$

$$\boldsymbol{g}_{jk} = \frac{1}{m_i \Omega_{jk}} \sum_p S_{jk}(\xi_p, \eta_p) M_p \boldsymbol{v}_p, \tag{16}$$

$$\boldsymbol{u}_{jk} = \boldsymbol{g}_{jk}/n_{jk}, \tag{17}$$

$$\bar{\bar{P}}_{jk} = \frac{1}{\Omega_{jk}} \sum_p S_{jk}(\xi_p, \eta_p) M_p (\boldsymbol{v}_p - \boldsymbol{u}_{jk})(\boldsymbol{v}_p - \boldsymbol{u}_{jk}), \tag{18}$$

$$\bar{\bar{T}}_{jk} = \bar{\bar{P}}_{jk}/n_{jk}. \tag{19}$$

Here, the summation index p applies to all particles of the given species, M_p is the macroparticle mass, and

$$\Omega_{jk} = \int\int S_{jk}(\xi, \eta) 2\pi r \left| \frac{\partial(z, r)}{\partial(\xi, \eta)} \right| d\xi d\eta, \tag{20}$$

is a volume associated to node jk, which takes cylindrical effects into consideration, thus avoiding errors at cells with small r.[20]

IV. WEIGHTING AT THE BOUNDARIES: THE BOHM CONDITION ISSUE

This is a small part of the PIC submodel but a difficult problem by itself, which justifies treating it in a separate section. The solutions of the (collisionless) electron-repelling sheath equations require necessarily that the ion flow satisfies the Bohm condition at the boundary with the quasineu-

tral plasma. For a Maxwell-Boltzmann electron distribution and a kinetic model for (singly charged) ions, the Bohm condition reads[21]

$$\left\langle \frac{1}{v_N^2} \right\rangle \equiv \frac{m_i}{n_e} \int_0^\infty dv_N \frac{f_i(v_N)}{m_i v_N^2} \leqslant \frac{m_i}{T_e}, \tag{21}$$

with n_e and T_e the local plasma density and electron temperature, $v_N = v \cdot 1_N$ the velocity perpendicular to wall and sheath, Fig. 1, and $f_i(v_N)$ the one-dimensional (1D) distribution function of ions (once the integrals along the two other components of v have been carried out). If the velocity dispersion of the ions can be neglected and u_i is the ion local *macroscopic* velocity, the Bohm condition takes the simple form $u_i \cdot 1_N \equiv u_{Ni} \geqslant \sqrt{T_e/m_i}$. For a steady-state solution and u_{Ni} subsonic far from the wall, the equal sign on the Bohm condition (21) must be used.

In continuous models of ions, the Bohm condition is implemented as a boundary condition on the quasineutral plasma. However, here ion dynamics are obtained from the motions of individual macroparticles and there is no direct way to impose a boundary condition on the ion flow. On the other hand, the electric potential, which affects the ion flow, is obtained through the electron fluid equations and the quasineutrality condition. The possibility of imposing an equivalent form of the Bohm condition in terms of the electric potential within the 2D electron submodel is unclear because of quasineutrality. We think that the quasineutral PIC solution should fulfill automatically the Bohm condition. The natural mechanism to achieve it would be the following: since an electron-repelling sheath does not return back any ions, the contour of the PIC domain acts as vacuum, which should force the ion flow to be sonic/supersonic there. The mechanism to establish this condition would be the propagation of ion-acoustic waves by the code, and the eventual blocking of the backwards wave.

We have investigated the fulfillment of the Bohm condition at the lateral walls in Ref. 13. The main conclusions and proposals of these works are summarized next.

(1) For usual mesh sizes, as the cell size of the mesh is reduced, the ion flow at the boundary increases significantly towards $n_e\sqrt{T_e/m_i}$ and larger plasma gradients over the whole radial section develop. However, for practical mesh sizes the ion flow remains well subsonic, making it evident that a different numerical approach should be used in order to satisfy the Bohm condition.

(2) The original version of HPHall used the same weighting function $S_{jk}(\xi, \eta)$, Eq. (14), to compute magnitudes at nodes placed along the domain boundaries, but substituting interval I by interval $J = I \cap D$, with D the simulation domain (see Fig. 6 of Ref. 13). This one-sided weighting tends to underestimate magnitudes that increase toward the wall such as the ion velocity. The error can be large for magnitudes that present large gradients near the sheath boundary (which include n_e, v_i, and ϕ, but not g_i).

(3) The correction of the one-sided weighting with an algorithm of higher order leads to a reasonable fulfillment of the Bohm condition if the mesh is fine enough.

(4) Alternatively, a way of satisfying directly the basic form of the Bohm condition, $u_{Ni} \geqslant \sqrt{T_e/m_i}$ was envisaged, yielding very good results even for relatively coarse meshes.

In HPHall-2, two algorithms are available for calculating plasma density at the computational boundary: either "correct weighting" or Bohm-condition forcing. Unless otherwise stated, Bohm-condition forcing was used in the calculations presented here. Both algorithms have been implemented at the lateral and rear (i.e., anode) walls. In order to explain these weighting schemes, we describe briefly how the plasma density at a node of the inner-wall boundary $(j,k)=(j,1)$ is determined.

The correct weighting algorithm is based on the fact that the linear one-sided weighting does not yield $n_e|_{\eta=1}$ but $n_e|_{\eta=4/3}$.[13] Assuming a linear variation of n_e within the cells adjacent to the nodes, HPHall-2 computes the density at the boundary as

$$n_e|_{\eta=1} = n_e|_{\eta=4/3} - \frac{1}{2}(n_e|_{\eta=2} - n_e|_{\eta=4/3}). \tag{22}$$

The validity of this weighting was demonstrated in Ref. 13. However, it was also found that, since most plasma profiles present large gradients near the sheath boundaries, fine meshes must be used in order to obtain these large gradient profiles (and satisfy the Bohm condition on the ion flow).

The second algorithm, Bohm-condition forcing, proposed by Ref. 13 defines the density at the boundary as

$$n_e|_{\eta=1} = \frac{g_{Ni}|_{\eta=1}}{v_{\text{Bohm}}}, \tag{23}$$

where g_{Ni} is the ion flux perpendicular to the wall and v_{Bohm} is the Bohm velocity. In the present formulation, g_{Ni} is obtained from the correct-weighting algorithm, and the Bohm velocity is defined simply as $v_{\text{Bohm}} = \sqrt{T_e|_{\eta=1}/m_i}$. Despite using such a simple expression for v_{Bohm}, Eq. (23) yields very good results even with coarse meshes.

Recently, a third algorithm based on surface weighting at the wall panels has been tested with good results.[14]

V. THE ELECTRON SUBMODEL

The axisymmetric macroscopic equations for the electrons correspond to the strongly magnetized, diffusive limit, which requires that $\omega_e \gg (\nu_e, D/Dt)$, where $\omega_e = eB/m_e$, ν_e is the effective collision frequency (defined below), and D/Dt is the electron total time derivative. The magnetic field introduces a large anisotropy in the transport properties of electrons. In order to take advantage of it, vector variables and equations for electrons are projected in the directions parallel and perpendicular (in a meridional plane) to the magnetic field, $1_\parallel$ and $1_\perp$, defined in Eq. (3) and shown in Fig. 1.

For the time interval $[t, t+\Delta t]$, the inputs to the electron subcode are the plasma and neutral densities, $n_e(z,r)$ and $n_n(z,r)$, and the ion flux density $g_i(z,r)$. The main outputs of the subcode are the new values of the electric potential and field, $\phi(z,r)$ and $E(z,r)$, and the electron temperature $T_e(z,r)$.

A. Ohm's and Fourier's laws

In the diffusive limit, the momentum equation reflects the equilibrium between the electric and magnetic forces, the electron pressure, and the resistive forces. In the magnetic-related reference frame, the three scalar momentum equations are

$$0 \simeq -\frac{\partial n_e T_e}{\partial \chi} + en_e\frac{\partial \phi}{\partial \chi}, \tag{24}$$

$$0 = -m_e(\omega_e g_{\perp e} + \nu_{en}g_{\theta e}) + F_{\theta,\text{ano}} + F_{\theta,\text{wall}}, \tag{25}$$

$$0 = -rB\frac{\partial n_e T_e}{\partial \lambda} + en_e rB\frac{\partial \phi}{\partial \lambda} + m_e\omega_e g_{\theta e}. \tag{26}$$

Here; $g_e = n_e u_e$ is the electron flux density; ν_{en} is the electron-neutral collision frequency (electron-ion collisions are disregarded); and $F_{\theta,\text{ano}}$ and $F_{\theta,\text{wall}}$ model the effects on the electron velocity of correlated plasma fluctuations (i.e., Bohm diffusion) and wall collisionality, respectively.[1,22] These two effects and the classical collisional forces are assumed smaller than the main forces, $|\nabla(n_e T_e) + en_e\nabla\phi|$, and have thus been neglected in Eqs. (24) and (26).

Janes and Lowder[23] showed that correlated fluctuations on the plasma density and the electric field leave an average azimuthal effect on the electrons, $F_{\theta,\text{ano}} \equiv \langle en_e'E_\theta'\rangle$, and suggested that this is proportional to the main, axial force. Then, using Eq. (26) to substitute the axial force by $m_e\omega_e g_{\theta e}$, one has[1]

$$F_{\theta,\text{ano}} \simeq -\alpha_{\text{ano}}\omega_e m_e g_{\theta e}, \tag{27}$$

with α_{ano} the proportionality constant, which represents the relative level of fluctuations. Since there is yet no established theory of this anomalous diffusion phenomenon, α_{ano} is taken as an empirical parameter.

Secondary electrons enter radially from the sheath into the quasineutral plasma as a monoenergetic beam with zero $E \times B$ (azimuthal) drift, which amounts to modify the electron mobility.[22] More precisely, the conversion at the walls of magnetized, primary electrons into unmagnetized, secondary electrons yields a net reduction over the macroscopic azimuthal velocity of the total electron population $u_{\theta e}$ which is modeled here as the resistive force

$$F_{\theta,\text{wall}} = -\nu_{wm} m_e g_{\theta e}, \tag{28}$$

with ν_{wm} an effective frequency. The adaptation of the formulation of Ahedo *et al.*[1] to oblique magnetic fields and the finite volume elements sketched in Fig. 1, yields the expression

$$\nu_{wm} = \frac{1}{\Delta V}\left[\frac{\Delta A}{n_e}\frac{g_{Ni}}{1-\delta_w}\right]_{S_3 \cup S_4} \tag{29}$$

with ΔV and ΔA meaning volume and lateral area and the SEE yield δ_w is defined in Sec. V B. Notice that SEE increases the electron mobility, as suggested by Morozov *et al.*[22] [The original HPHall included a different and incomplete formulation of wall collisionality. A wall current was computed based on the net axial drift of secondary electrons after leaving the sheath and that wall current was taken into account only when computing the discharge current, i.e., in Eq. (39)]

Defining

$$\nu_e = \nu_{en} + \nu_{wm} + \alpha_{\text{ano}}\omega_e \tag{30}$$

as the total momentum collision frequency, Eq. (25) becomes

$$0 \simeq -\omega_e g_{\perp e} - \nu_e g_{\theta e}, \tag{31}$$

which relates $g_{\theta e}$ and $g_{\perp e}$. Substituting $g_{\theta e}$ into Eq. (26) one has

$$eg_{\perp e} = \frac{r\nu_e}{\omega_e}\left(-\frac{\partial n_e T_e}{\partial \lambda} + en_e\frac{\partial \phi}{\partial \lambda}\right), \tag{32}$$

which is Ohm's law for the electron motion across B lines.

The vector equation for heat conduction q_e is treated similarly to the momentum equation. After some algebraic manipulation the heat conduction equation in the diffusive limit reduces to[1]

$$0 \simeq -\omega_e q_{\perp e} - \nu_e q_{\theta e}, \tag{33}$$

$$q_{\perp e} = -\frac{5}{2}n_e T_e\frac{r\nu_e}{e\omega_e}\frac{\partial T_e}{\partial \lambda}, \tag{34}$$

$$0 \simeq -\frac{\partial T_e}{\partial \chi}. \tag{35}$$

Equation (33) relates $q_{\theta e}$ (diamagnetic component of the heat conduction) and $q_{\perp e}$, Eq. (34) is Fourier's law for the perpendicular dynamics, and Eq. (35) states that T_e is constant along any magnetic streamline.

Using this last result, we obtain a first integral of Eq. (24),

$$e\phi(\lambda,\chi) = e\phi^*(\lambda) + T_e(\lambda)\ln\frac{n_e(\lambda,\chi)}{n_0}, \tag{36}$$

where ϕ^* is called the thermalized electric potential[22] and n_0 is a convenient constant (which affects the value of ϕ^* but not of ϕ).

The substitution of ϕ into Ohm's law (32) yields

$$g_{\perp e} = n_e\frac{r\nu_e}{e\omega_e}\left[\left(\ln\frac{n_e}{n_0}-1\right)\frac{\partial T_e}{\partial \lambda} + e\frac{\partial \phi^*}{\partial \lambda}\right], \tag{37}$$

which relates $g_{\perp e}$ to the derivatives of $T_e(\lambda)$ and $\phi^*(\lambda)$.

B. Conservation of particles and energy

The conservation equation for the electrical current can be written as

$$\nabla \cdot (g_i - g_e) = 0. \tag{38}$$

HPHall-2 admits only dielectric materials at lateral walls. In that case, the integration of Eq. (38) across any streamsurface connecting the inner and outer walls, $S:\lambda=\text{const.}$, yields, at a given time,

$$-I_e(\lambda) = I_d - I_i(\lambda), \tag{39}$$

where $I_\alpha(\lambda) = \int_S eg_{\perp\alpha}dS, (\alpha=i,e)$, are the species electrical currents, and I_d is the discharge current (independent of λ). Using now Eq. (37) one has

$$e\frac{\partial\phi^*}{\partial\lambda}\int_S n_e\frac{rv_e}{\omega_e}dS = \frac{\partial T_e}{\partial\lambda}\int_S n_e\frac{rv_e}{\omega_e}\left(1-\ln\frac{n_e}{n_0}\right)dS + I_i(\lambda)$$
$$- I_d, \qquad (40)$$

which yields $\partial\phi^*/\partial\lambda$ in terms of $\partial T_e/\partial\lambda$ and I_d. The ion current $I_i(\lambda)$ comes from the PIC calculation.

Finally, the electron energy equation is written as

$$\frac{\partial}{\partial t}\left(\frac{3}{2}n_eT_e\right) + \nabla\cdot\hat{\boldsymbol{q}}_e = -e\boldsymbol{g}_e\cdot\boldsymbol{E} - \dot{n}_i\alpha_iE_i, \qquad (41)$$

where $\hat{\boldsymbol{q}}_e=\frac{5}{2}T_e\boldsymbol{g}_e+\boldsymbol{q}_e$ is the total (convective plus conductive) flux of enthalpy, and

$$\alpha_i(T_e/E_i) = 2.0 + 0.254\exp(0.677E_i/T_e) \qquad (42)$$

is Dugan's expression of the ionization cost factor (for xenon), which takes into account excitation/radiation processes.[7] Electron energy losses due to elastic collisions are much lower than the Joule heating and have been disregarded in Eq. (41).

A partial differential equation for $T_e(\lambda,t)$ is obtained by integrating the energy equation on finite volume elements centered on the magnetic mesh streamlines λ_l. Using the nomenclature of Fig. 1, one has

$$\int_{\Delta V}dV\left(\frac{3}{2}\frac{\partial n_eT_e}{\partial t} - eg_{\perp e}rB\frac{\partial\phi}{\partial\lambda} + \dot{n}_i\alpha_iE_i\right) + \int_{S_3\cup S_4}\hat{q}_{NeQ}dS$$
$$= -\int_{S_1\cup S_2}\hat{q}_{\perp e}1_\perp\cdot d\boldsymbol{S}, \qquad (43)$$

where $d\boldsymbol{S}$ point outwards from the volume element,

$$\hat{q}_{\perp e} = \frac{5}{2}n_eT_e\frac{rv_e}{e\omega_e}\left[\left(\ln\frac{n_e}{n_0}-2\right)\frac{\partial T_e}{\partial\lambda} + e\frac{\partial\phi^*}{\partial\lambda}\right], \qquad (44)$$

and $\hat{q}_{NeQ}\equiv\hat{\boldsymbol{q}}_{eQ}\cdot 1_N$ measures the energy density flux at a lateral boundary, which in most cases correspond to a sheath edge. The work of the electric field along the magnetic lines $eg_{\|e}\partial\phi/\partial\chi$ has been neglected in Eq. (43) since it is much smaller than both $\hat{q}_{NeQ}$ and the work of the perpendicular component $E_\perp$. (An additional, practical reason to disregard it, is to avoid the cost of computing $g_{\|e}$ and $\partial\phi/\partial\chi$ at each electron time step.)

For the dielectric walls, we implement the sheath model of Ahedo,[15] which, completing the model of Fife *et al.*,[9] (i) takes into account the sheath charge saturation at high SEE yields,[24,25] and (ii) makes consistent the presence of primary (*p*) and secondary (*s*) electrons within the sheath with a single electron population (*e*) in the bulk of the plasma. The energy density fluxes at the wall and sheath-edge boundaries (named points *W* and *Q*, respectively) satisfy[15]

$$\hat{q}_{NeW} \simeq \frac{2T_p}{1-\delta_w(T_p)}g_{Ni}, \quad \hat{q}_{NeQ} = \hat{q}_{NeW} + e\phi_{WQ}g_{Ni}, \qquad (45)$$

where g_{Ni} is the ion density flux across the sheath, ϕ_{WQ} is the potential fall in the sheath, and $\delta_w(T_p)$ the effective SEE yield in terms of the temperature of primary electrons. For the cases computed here we took $\delta_w(T_p) = \min\{(T_p/T_1)^{0.576}, 0.983\}$, with $T_1=26.4$ eV; the value

$\delta_w=0.983$ corresponds to the charge-saturation regime. Expressions relating ϕ_{WQ} and T_p to the parameters n_{eQ}, T_{eQ}, and g_{Ni}, of the quasineutral plasma, were taken from Ref. 15.

C. Integration procedure

The substitution of Eqs. (34), (36), (37), and (40), into Eq. (43) yields an integral equation involving only $T_e(\lambda,t)$, its derivatives, and parameters and variables that are given by the PIC submodel. Equation (1) provides the variable transformation needed to solve the volume and surface integrals. Volume integrals use the value of the integrand at the intermediate surface $S:\lambda=\lambda_l$, Fig. 1. Thus, Eq. (43) is transformed into

$$\left[C_1 + C_2\frac{\partial T_e}{\partial t} + C_3T_e\frac{\partial T_e}{\partial\lambda} + C_4\left(\frac{\partial T_e}{\partial\lambda}\right)^2\right]_S$$
$$= \left(C_5T_e + C_6T_e\frac{\partial T_e}{\partial\lambda}\right)_{S_1} + \left(C_7T_e + C_8T_e\frac{\partial T_e}{\partial\lambda}\right)_{S_2}, \qquad (46)$$

where the coefficients C_j, $(j=1,\ldots,8)$ are integrals involving plasma variables at S, S_1, or S_2; for instance $C_2(\lambda)=(3/2)\int_{\Delta V}n_edV$, and $C_5(\lambda)=(5/2e)[I_d-I_i(\lambda)]$.

The discretization of Eq. (46) leads to a finite-differences evolution equation for T_e at the selected mesh of λ_l lines.[7] Due to numerical stability, these equations must be integrated in a subloop with smaller time step δt. The size of this electron time step is, typically, $\delta t\sim 10^{-3}-10^{-2}\Delta t$, where Δt is the time step used to integrate the PIC model. However, the coefficients C_j, $\phi^*(\lambda)$ [Eq. (40)] and $\phi(\lambda,\chi)$ [Eq. (36)], although dependent on T_e, are computed only once for the whole interval Δt.

Finally, the discharge potential between the point representing the cathode and the anode, $V_d(I_d)$, is obtained from

$$V_d = \left[\phi^* - \frac{T_e}{e}\ln\frac{Aen_0\sqrt{T_e/2\pi m_e}}{I_d-I_i}\right]_{\lambda=\lambda_1}, \qquad (47)$$

where the cathode potential has been set to zero, and the potential drop at the anode sheath has been taken into account (for electron-repelling sheaths). Generally, V_d is an input parameter and the discharge current is an output parameter. Then Newton's iteration algorithm is used on Eq. (47) to determine I_d at each time step. In each iteration, Eq. (46) is integrated for the time step Δt; in general, 2 or 3 of these iterations are enough to converge to the given value of V_d.

VI. RESULTS

This section presents computational results obtained for three cases, named 1.1, 1.2, and 2. Operational conditions and (time-averaged) performances are listed in Table I. Cases 1.1 and 1.2 simulate the SPT-70 thruster as modeled by Fife[7] and sketched in Fig. 1. Case 1.1 was run with the original HPHall and Case 1.2 with HPHall-2. Their plasma response is compared in Figs. 2 and 3; spatial plots correspond to time-averaged values, excluding the initial, transient period. Figures 4–9 are for Case 2, which corresponds to the same thruster geometry and magnetic field topology defined in Fig.

TABLE I. Performances for cases 1.1, 1.2, and 2. Case 1.1 uses the original HPHall, case 1.2 uses the modified HPHall-2. Both cases 1.1 and 1.2 refer to the same thruster and operating conditions (V_d, $\dot{m}$). The magnetic lines are as in Fig. 1(b). The magnetic field magnitude has a maximum of 350 G near the exit of the channel and has a value of around 10 G at the anode. Case 2 is run in HPHall-2, and uses a simplified, purely radial B field. The magnetic field has a maximum of 270 G near the exit of the channel and a value of around 10 G at the anode.

	Case 1.1	Case 1.2	Case 2
$\dot{m}$	2.30 mg/s	2.29 mg/s	2.31 mg/s
I_d	2.23 A	2.05 A	1.80 A
$I_d V_d$	623 W	573 W	535 W
P_{wall}	106 W	144 W	206 W
P_{ion}	53 W	55 W	64 W
P_{anode}	15 W	34 W	27 W
P_{use}	449 W	340 W	238 W
F	34 mN	30 mN	29 mN
I_{sp}	1508 s	1340 s	1280 s
η	41%	35%	33%
η_u	86%	76%	71%

1 of Ref. 13. This case uses a simple geometry and takes $B_z=0$ (violating irrotationality), with the intentions of (i) isolating and interpreting more easily 2D effects due to the plasma-wall interaction, (ii) interpreting more easily the results, and (iii) comparing with the macroscopic model of Ahedo *et al.*[1] The three cases are just examples to show the capabilities of the model; no study has been made here in order to adjust empirical parameters or optimize thruster performances.

Figures 2 and 3 compare 2D contour maps of the main plasma magnitudes for cases 1.1 and 1.2. The irrotational magnetic field is plotted in Fig. 1; it presents a peak value of 350 G near the exit of the channel, a value of the order of 10 G at the anode, and magnetic lines are rather symmetrical with respect to the channel median. The fulfilment of the Bohm condition at the sheath edges in case 1.2 explains most of the differences with case 1.1. Thus, as ion velocities are forced to be very similar at the two lateral sheath edges, plasma profiles are more symmetrical with respect to the channel median. Second, larger ion radial velocities mean larger radial gradients of density and potential (for example, the radial drop of n_e at the maximum density section is 30% larger with the new model); as a consequence, equipotential lines follow less closely the magnetic lines. Third, plasma recombination at lateral walls is larger, leading to larger neutral densities near the walls and, eventually, a lower propellant utilization and thrust efficiency (Table I). Four, the ful-
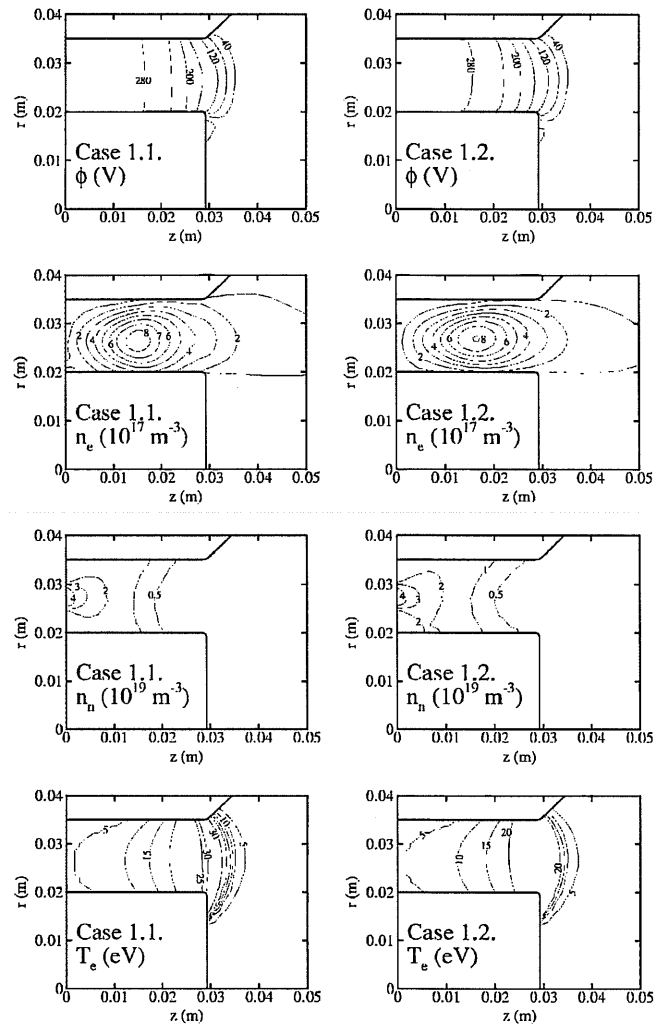

FIG. 2. Two-dimensional maps of plasma magnitudes for cases 1.1 and 1.2.

filment of the Bohm condition at the anode sheath edge, leads to a larger reduction of n_e near the anode and the presence of a well-defined ion backstreaming region, as observed experimentally by Bishaev and Kim[26] and theoretically by Ahedo *et al.*[1] The different electron temperature profiles in Fig. 2 are mainly due to a different treatment of the external walls of the channel. HPHall-2 treats them as dielectrics instead of as vacuum. This increases the energy losses in the near plume, thus reducing the maximum plasma temperature.

Figures 4-9 for case 2 complete results shown in Ref. 13 on the fulfillment of the Bohm condition at the lateral walls. Figure 4 illustrates the consequences of this fulfillment at the anode sheath edge. Notice the larger ion velocities there and
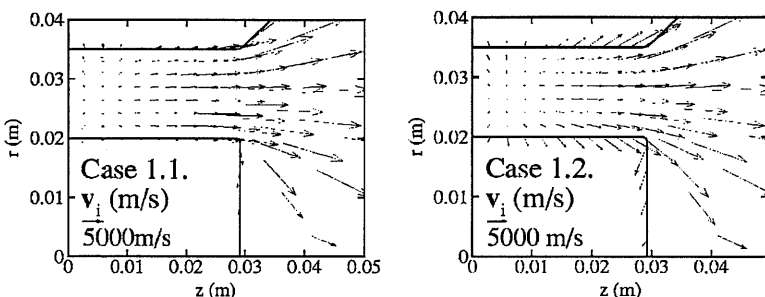

FIG. 3. Ion velocity vectors (projected on a meridional plane) for cases 1.1. and 1.2. At the chamber boundaries, the vectors do not include the velocity increment within the adjacent sheaths (for instance, a sheath potential of 50 V increases the ion radial velocity by about 8 km/s).
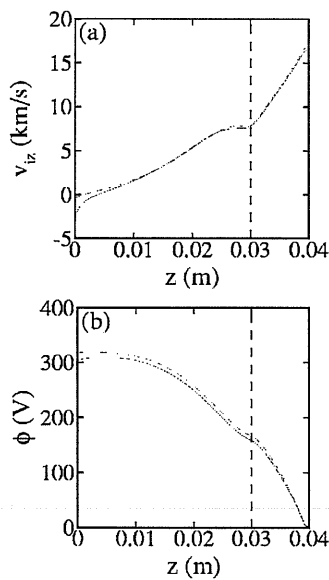
FIG. 4. Case 2. Effects of correcting the weighting of ion magnitudes at the anode boundary. The vertical dashed line represents the exit of the chamber. Solid and dashed lines correspond to the present and original models, respectively. Axial profiles at $r=0.027$ m of (a) the ion axial velocity and (b) the electric potential.

FIG. 6. Case 2. Axial profiles of the electron temperature T_e the potential drop at the outer sheath ϕ_{WQ} energy losses at the walls of ions and electrons, $Q_{wall,i}$ and $Q_{wall,e}$, and excitation and ionization losses Q_{ion}. The electron temperature for 100% yield is $T_1=26.4$ eV.

the displacement of the location of the maximum electric potential away from the anode. In these simulations, the improved treatment of the near-anode region has important effects locally but a weak global effect on thruster performances. The relevance of the near-anode zone for more general thruster conditions remains to be studied.

Figure 5 shows the ion and neutral flows at different axial locations along the chamber, $\dot{m}_i(z)$ and $\dot{m}_n(z)$. The sum of both is the total mass flow $\dot{m}(z)$, which is practically conserved inside the thruster and equal to $\dot{m}_A$. This conservation check was needed, since the PIC model uses different algorithms for creation/destruction of macroneutrals and macroions [for instance, see Eqs. (7) and (8) for ionization]. The defect of neutrals in the near plume is due to mass losses through the lateral plume boundaries. The reverse ion flow to the anode is about a 1.2% of the emitted mass flow $\dot{m}_A$. The dashed line of Fig. 5 plots the cumulative ion losses due to recombination at the lateral walls, $\dot{m}_{i,wall}(z)$. As we showed in Ref. 13, for case 2, the correct weighting algorithm at the boundaries increases the ion losses to the lateral walls by a factor of 2.2 with respect to the original model. Total ion losses to the walls amount to 49% of $\dot{m}_A$, which agrees rather
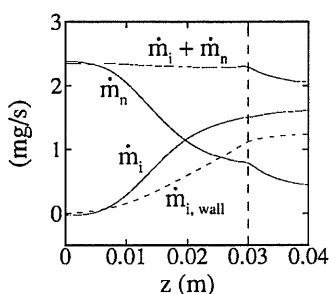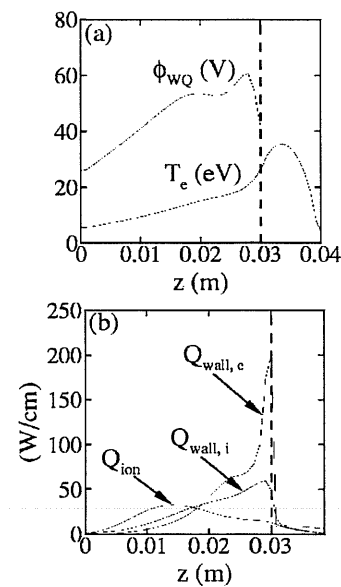

FIG. 5. Case 2. Axial variation of ion and neutral flows. The dashed line shows the cumulative ion flow lost to the lateral walls.

well with data reported in Refs. 26 and 27. Finally, we notice that the inclusion of CEX collisions does not modify practically the thruster performances in our simulations.

Two-dimensional contours of the electric potential, the plasma density, and the neutral density for case 2 were shown in Fig. 11 of Ref. 13. Here, Fig. 6(a) shows the electron temperature $T_e(z)$ and the potential drop at the outer lateral sheath $\phi_{WQ}(z)$. For the evolution of $\phi_{WQ}(z)$, with T_e and the SEE material properties see Ref. 15 (in particular observe the sheath potential fall in the charge-saturation regime). Figure 6(b) plots the axial distribution of three power losses: ionization and lateral-wall heating by ion and electron impacts; $Q_{wall,e}$ and $Q_{wall,i}$ have taken into account the energy exchanges across the sheaths. In the near plume the inwards electron flow is Joule heated. At the chamber exit, the large electron temperature brings the SEE yield to 95%; thus, the lateral sheaths are near charge saturation, electron energy losses dominate over Joule heating and cool the electron fluid. Heat conduction effects are responsible for placing the electron temperature peak outside the chamber instead of at the exit (a situation reported experimentally by Raitses et al.[28]). Similar temperature profiles are obtained with the macroscopic model of Ahedo et al.,[1] who showed how the combination of heat conduction and high wall energy losses induced by SEE, limit effectively the maximum T_e: a simple balance of enthalpy flow and Joule heating would lead to peak electron temperatures of order 2 $eV_d/5$, in this case 120 eV. Figure 6(b) illustrates the high sensitivity of wall losses to the electron temperature and the comparatively low value of ionization losses. For case 2, energy wall losses represent 39% of the available power, and ionization losses a mere 12%. The useful power, computed as the total energy flow of heavy species at the downstream end of the domain, amounts to 44%.

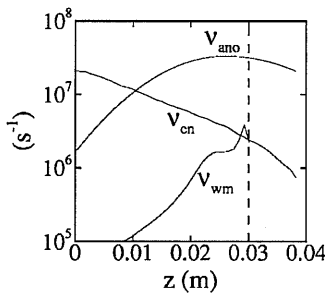Figure 7 compares the different contributions to the ef-

FIG. 7. Case 2. Axial profiles of the different contributions to the total collision frequency of the electron fluid at the channel radial midsection. $\nu_{ano} = \alpha_{ano}\omega_e$, with $\alpha_{ano} = 1/80$, represents Bohm-type diffusion.

fective electron collision frequency, $\nu_e(z)$ in Eq. (30), at different axial locations. In agreement with results from macroscopic simulations[1] wall collisionality has a marginal role on cross-field transport, even at the chamber exit, where SEE is about 95%. Classical collisions dominate near the anode and fluctuation-based diffusion in the rest of the chamber, which coincides with the experimental observations by Meezan and Capelli.[29] Wall collisionality could be more relevant at high-potential operation, where secondary electron effects are even larger than here, or if the anomalous diffusion is damped in the chamber exit zone, as some authors suggest.[29,30]

Figure 8(a) plots the scalar ion temperature (indeed, velocity dispersion), $T_i = \mathrm{trace}(\overline{\overline{T_i}})/3$, as computed from the temperature tensor $\overline{\overline{T_i}}$. The main contribution comes from the component zz: $T_i \sim T_{zz,i}/3$. The high value of this velocity dispersion contrasts with the results of the steady model of Ref. 1. The explanation is that the dispersion here is caused mainly by the large temporal fluctuations of the electric potential at any spatial location, and marginally by the extended ionization region. These fluctuations are illustrated in Fig. 8(b), which plots the temporal variation of ϕ at a particular point of the channel exit, and shows oscillations of 50 V
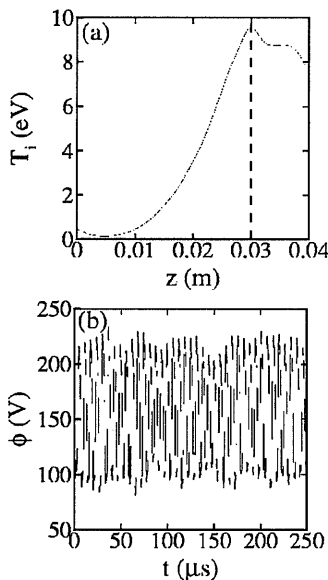

FIG. 8. Case 2. (a) Axial profile of the ion scalar temperature. (b) Temporal behavior of the electric potential at $z = 0.03$ m and $r = 0.0275$ m.
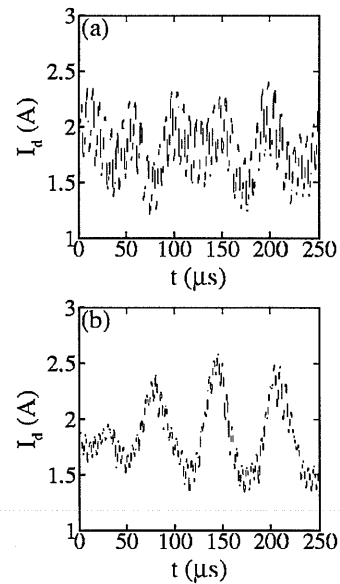

FIG. 9. Case 2. Temporal evolution of the discharge current when (a) the Bohm condition forcing or (b) the corrected weighting algorithm are used.

over a mean value of ~ 150 V. This electric potential oscillations have an amplitude larger than expected, probably due to numerical effects. Thus, the ion temperature reaches values over the experimental results. Further study needs to be done to understand the oscillations observed in the model.

Simulation models are expected to be useful to understand the mechanisms setting up the large variety of plasma oscillations arising in Hall thrusters. At the same time, caution must be used in order to distinguish physical fluctuations from numerical ones. Figures 9(a) and 9(b) illustrate these two aspects of the problem. The two curves plot the temporal variation of the discharge current when using either the correct-weighting or Bohm-condition forcing algorithms at the domain boundaries. In both curves we identify a main oscillation mode of ~ 16 kHz and a high-frequency mode of ~ 150 kHz. No investigation has been made on the nature of these fluctuations, but it is very likely that the two modes correspond to the well-reported, breathing, and ion-transit instabilities, respectively.[2] On the other hand, the two curves of Fig. 9 demonstrate that the fluctuation level can be strongly influenced by numerical algorithms (by the weighting at the boundaries, in this case). The relative amplitude of the high-frequency mode is 15% when applying the Bohm-condition forcing and just 5% with the correct-weighting algorithm. The amplitude of the main mode is also slightly higher with the Bohm-condition forcing. This algorithm seems to induce higher amplitude oscillations, maybe because the PIC submodel is "forced" to reach the average velocity $\sqrt{T_e/m_i}$, which is not an information obtained from the PIC submodel, but from the sheath model. This gives the algorithm an "extrinsic" character.

VII. CONCLUSIONS

We have presented the main aspects of a 2D hybrid model, capable of performing quick and detailed simulations of the discharge in a conventional Hall thruster geometry. The code is aimed for basic studies such as (i) the sensitivity

of the discharge to the operational, semiempirical, and numerical parameters, and to the magnetic field topology, (ii) plasma-wall interaction effects(including erosion analysis[31]), (iii) local energy balances (among energy convection and conduction, Joule heating, and ionization and wall losses), and (iv) electron transport.

The paper emphasizes the recent improvements on the model, which highlight the importance of physical and mathematical aspects of the interaction among the (quasineutral) plasma, the sheaths, and the walls. In particular, the fulfilment of the Bohm condition at the sheath edge is found to affect strongly the plasma profiles and the plasma recombination at the walls.

The new code is more consistent with our present understanding of Hall thruster physics but it does not always present a better agreement with experimental results. Whereas good results are obtained for the ion current collected by lateral walls, the propellant utilization seems to be lower than in experiments (which, in the end, results in a modest thrust efficiency). In addition, energy losses at the walls seem to be overestimated. Recent publications[32–36] are working with the idea of a partial thermalization of the (primary and secondary) electron distribution function, which would reduce wall energy losses and affect the ionization rate (through changes on the temperature field). Also, doubly charged ions are known to increase the propellant utilization even at moderate discharge voltages.[31]

A relevant element of the model responsible for matching thruster performance to experimental data, is electron cross-field diffusion. Some of the differences detected between the code and the experiments are probably due to the not yet well-understood anomalous diffusion. To use HPHall-2 in a performance prediction role, the next step would be to develop self-consistent electron diffusion models[37] and to implement and validate them in the framework of HPHall-2.

ACKNOWLEDGMENTS

[1] E. Ahedo, J. Gallardo, and M. Martínez-Sánchez, Phys. Plasmas **10**, 3397 (2003); **9**, 4061 (2002); E. Ahedo, P. Martínez-Cerezo, and M. Martínez-Sánchez, *ibid.* **8**, 3058 (2001).
[2] S. Barral, K. Makowski, Z. Peradzynski, N. Gascon, and M. Dudeck, Phys. Plasmas **10**, 4137 (2003).
[3] J. J. Szabo, Ph.D. thesis, Massachusetts Institute of Technology, 2001.
[4] J. Fife and M. Martínez-Sánchez, in *Proceedings of the 24th International Electric Propulsion Conference, Moscow, Russia* (Electric Rocket Propulsion Society, Fairview Park, Ohio, 1995), IEPC 95–240.
[5] J. Boeuf and L. Garrigues, J. Appl. Phys. **84**, 3541 (1998).
[6] G. Hagelaar, J. Bareilles, L. Garrigues, and J. Boeuf, J. Appl. Phys. **91**, 5592 (2002).
[7] J. M. Fife, Ph.D. thesis, Massachusetts Institute of Technology, 1998.
[8] J. Fife and M. Martinez-Sanchez, in *Proceedings of the 32nd Joint Propulsion Conference, Lake Buena Vista, FL* (American Institute of Aeronautics and Astronautics, Washington, DC, 1996), AIAA 96–3197.
[9] J. Fife, M. Martínez-Sánchez, and J. Szabo, in *Proceedings of the 33rd Joint Propulsion Conference, Seattle, WA* (American Institute of Aeronautics and Astronautics, Washington, DC, 1997), AIAA 97–3052.
[10] J. Szabo, M. Martínez-Sánchez, and J. Monheiser, in *Proceedings of the 34th Joint Propulsion Conference, Cleveland, OH* (American Institute of Aeronautics and Astronautics, Washington, DC, 1998), AIAA 98–3795.
[11] S. Locke, U. Shumlak, and J. Fife, in *Proceedings of the 27th International Electric Propulsion Conference, Pasadena, CA* (Electric Rocket Propulsion Society, Fairview Park, OH, 2001), IEPC 01–23.
[12] S. Cheng and M. Martínez-Sánchez, in *Proceedings of the 40th Joint Propulsion Conference, Fort Lauderdale, FL* (American Institute of Aeronautics and Astronautics, Washington, DC, 2004), AIAA 2004–3635.
[13] F. Parra and E. Ahedo, in *Proceedings of the 40th Joint Propulsion Conference, Fort Lauderdale, FL* (American Institute of Aeronautics and Astronautics, Washington, DC, 2004) AIAA 2004–3955; F. Parra, E. Ahedo, M. Martínez-Sánchez, and J. Fife, in *SP-555: 4th Spacecraft Propulsion Conference, Sardinia (Italy)* (European Space Agency, Noordwijk, The Netherlands, 2004).
[14] D. Escobar, E. Ahedo, and F. I. Parra, in *Proceedings of the 29th International Electric Propulsion Conference, Princeton* (Electric Rocket Propulsion Society, Fairview Park, OH, 2005), IEPC 2005–041.
[15] E. Ahedo, Phys. Plasmas **9**, 4340 (2002).
[16] C. Birdsall and A. Langdon, *Plasma Physics via Computer Simulation* (Institute of Physics, Bristol, 1991).
[17] G. Bird, *Molecular Gas Dynamics and the Direct Simulation of Gas Flows* (Clarendon, Oxford, 1994).
[18] *Partially Ionized Gases*, edited by M. Mitchner and C. H. Kruger, Jr. (Wiley, New York, 1973).
[19] M. Celik, M. Santi, S. Cheng, M. Martínez-Sánchez, and J. Peraire, in *Proceedings of the 28th International Electric Propulsion Conference, Toulouse, France* (Electric Rocket Propulsion Society, Fairview Park, OH, 2003), IEPC-03-134.
[20] J. Verboncoeur, J. Comput. Phys. **174**, 421 (2001).
[21] E. Harrison and W. Thompson, Proc. Phys. Soc. London **74**, 145 (1959).
[22] A. Morozov, Y. Esipchuk, G. Tilinin, A. Trofimov, Y. Sharov, and G. Y. Shchepkin, Sov. Phys. Tech. Phys. **17**, 38 (1972).
[23] G. Janes and R. Lowder, Phys. Fluids **9**, 1115 (1966).
[24] G. Hobbs and J. Wesson, Plasma Phys. **9**, 85 (1967).
[25] L. Jolivet and J.-F. Roussel, in *SP-465: 3rd Spacecraft Propulsion Conference, Cannes (Francia)* (European Space Agency, Noordwijk, The Netherlands, 2000), pp. 367–376.
[26] A. Bishaev and V. Kim, Sov. Phys. Tech. Phys. **23**, 1055 (1978).
[27] V. Kim, J. Propul. Power **14**, 736 (1998).
[28] Y. Raitses, D. Staack, M. Keidar, and N. J. Fisch, Phys. Plasmas **12**, 057104 (2005).
[29] N. Meezan, W. Hargus, and M. Capelli, Phys. Rev. E **63**, 026410 (2001).
[30] M. K. Allis, N. Gascon, C. Vialard-Goudou, M. A. Cappelli, and E. Fernandez, in *Proceedings of the 40th Joint Propulsion Conference, Fort Lauderdale, FL* (American Institute of Aeronautics and Astronautics, Washington, DC, 2004), AIAA 2004–3951.
[31] D. Escobar, A. Antón, and E. Ahedo, in *Proceedings of the 29th International Electric Propulsion Conference, Princeton* (Electric Rocket Propulsion Society, Fairview Park, OH, 2005), IEPC 2005–040.
[32] N. Meezan and M. Capelli, Phys. Rev. E **66**, 036401 (2002).
[33] K. Sullivan, J. Fox, O. Batischev, and M. Martínez-Sánchez, in *Proceedings of the 40th Joint Propulsion Conference, Fort Lauderdale, FL* (American Institute of Aeronautics and Astronautics, Washington, DC, 2004), AIAA 2004–3777.
[34] E. Ahedo and F. Parra, Phys. Plasmas **12**, 073503 (2005).
[35] E. Ahedo, V. de Pablo, and M. Martínez-Sánchez, in *Proceedings of the 29th International Electric Propulsion Conference, Princeton* (Electric Rocket Propulsion Society, Fairview Park, OH, 2005), IEPC 2005–118.
[36] D. Sydorenko, A. Smolyakov, I. Kaganovich, and Y. Raitses, Phys. Plasmas **13**, 014501 (2006).
[37] J. Gallardo and E. Ahedo, in *Proceedings of the 29th International Electric Propulsion Conference, Princeton* (Electric Rocket Propulsion Society, Fairview Park, OH, 2005), IEPC 2005–117.